



THE UNIVERSITY *of* EDINBURGH

Edinburgh Research Explorer

Human contribution to the risk of 2021 Northwestern Pacific concurrent marine and terrestrial summer heat

Citation for published version:

Tang, H, Wang, J, Chen, Y, Tett, S, Sun, Y, Chen, L, Sparrow, S & Dong, B 2023, 'Human contribution to the risk of 2021 Northwestern Pacific concurrent marine and terrestrial summer heat', *Bulletin of the American Meteorological Society*, pp. E673–E679. <https://doi.org/10.1175/BAMS-D-22-0238.1>

Digital Object Identifier (DOI):

[10.1175/BAMS-D-22-0238.1](https://doi.org/10.1175/BAMS-D-22-0238.1)

Link:

[Link to publication record in Edinburgh Research Explorer](#)

Document Version:

Peer reviewed version

Published In:

Bulletin of the American Meteorological Society

General rights

Copyright for the publications made accessible via the Edinburgh Research Explorer is retained by the author(s) and / or other copyright owners and it is a condition of accessing these publications that users recognise and abide by the legal requirements associated with these rights.

Take down policy

The University of Edinburgh has made every reasonable effort to ensure that Edinburgh Research Explorer content complies with UK legislation. If you believe that the public display of this file breaches copyright please contact openaccess@ed.ac.uk providing details, and we will remove access to the work immediately and investigate your claim.



1 **Human contribution to the risk of 2021 Northwestern Pacific**
2 **concurrent marine and terrestrial summer heat**

3 Haosu Tang^{1,7}, Jun Wang^{1*}, Yang Chen², Simon F. B. Tett³, Ying Sun⁴, Lijing Cheng¹,
4 Sarah Sparrow⁵, and Buwen Dong⁶

5 ¹*State Key Laboratory of Numerical Modeling for Atmospheric Sciences and Geophysical Fluid*
6 ²*Dynamics (LASG) / Key Laboratory of Regional Climate Environment for Temperate East Asia*
7 ³*(RCE-TEA) / International Center for Climate and Environment Sciences (ICCES), Institute of*
8 ⁴*Atmospheric Physics, Chinese Academy of Sciences, Beijing, China*

9 ⁵*State Key Laboratory of Severe Weather, Chinese Academy of Meteorological Sciences, Beijing,*
10 ⁶*China*

11 ⁷*School of Geosciences, University of Edinburgh, Edinburgh, UK*

12 ⁸*National Climate Center, Laboratory for Climate Studies, China Meteorological*
13 ⁹*Administration, Beijing, China*

14 ¹⁰*Oxford e-Research Centre, Department of Engineering Science, University of Oxford, Oxford,*
15 ¹¹*UK*

16 ¹²*National Centre for Atmospheric Science, Department of Meteorology, University of Reading,*
17 ¹³*Reading, UK*

18 ¹⁴*University of Chinese Academy of Sciences, Beijing, China*

19 *Correspondence to wangjun@tea.ac.cn

20

21

22

23

24

25

26

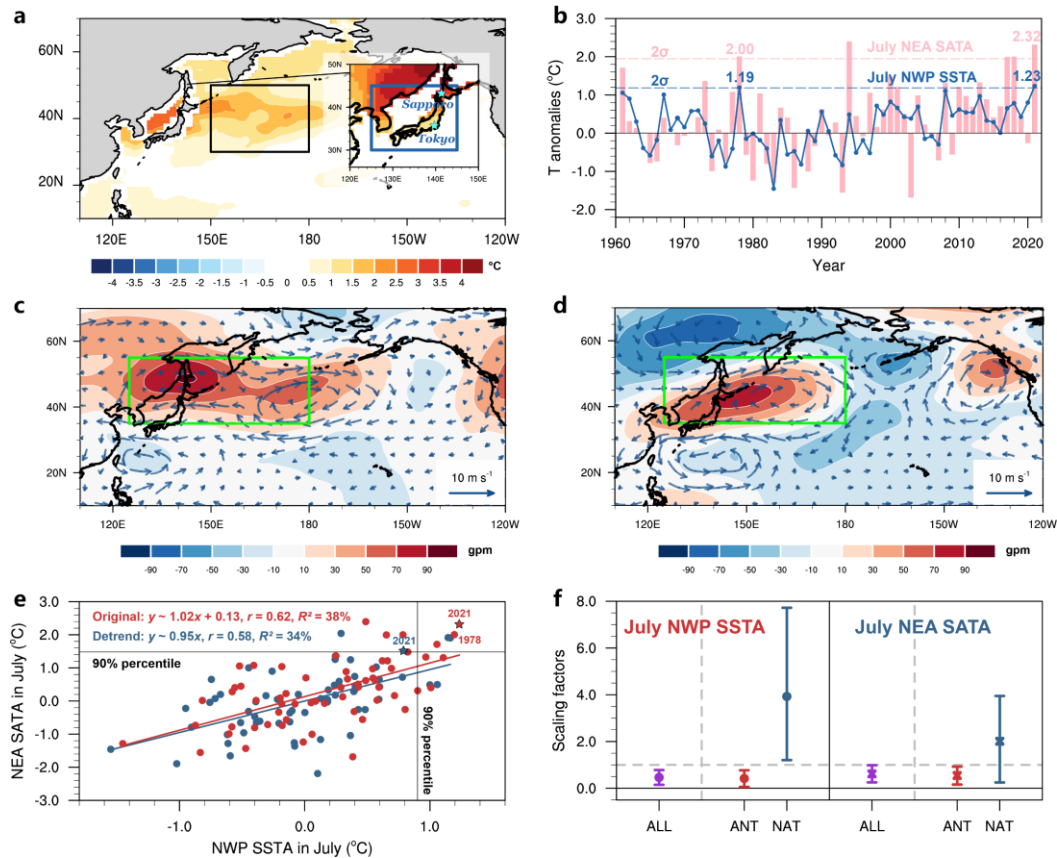
27

28

29

30 *Capsule Summary:* Current human-induced warming has led to approximately a 30-
31 fold increase in the occurrence probability of 2021 Northwestern Pacific concurrent
32 marine and terrestrial summer heat.

33 *Introduction.* July 2021 was the warmest month ever recorded for the globe, during
34 which several extreme weather events occurred (NOAA, 2022). Less noticed but as
35 important, an unprecedentedly intense marine heatwave impacted broad swaths of the
36 Northwestern Pacific (NWP; black box in Fig. 1a; 150–180°E; 30–50°N), in the same
37 month, with regional mean sea surface temperature anomalies (SSTA; relative to 1961–
38 1990) up to 1.23°C (Kuroda and Setou 2021). This marine heat caused an
39 unprecedented outbreak of red tides off Hokkaido and decimated the local fishery
40 industry, with direct damages totaling approximately \$150 million (Kuroda et al. 2021).
41 In the meantime, neighboring Northeast Asia (NEA; blue box in Fig. 1a; 125–145°E;
42 30–45°N) experienced extreme terrestrial heat, with regional mean surface air
43 temperature anomalies (SATA) reaching 2.32°C, making the Tokyo 2020 Olympics the
44 hottest Games in history. This spatially concurrent marine and terrestrial heat may cause
45 regionally compounding effects, including synchronous reductions in fishery and
46 agricultural yields and potential impacts on food security (Zscheischler et al. 2020).
47 This spatially compounding heat likely results from a persistent blocking high. It
48 remains poorly understood concerning human influences on the occurrence risk of this
49 compound event. The goal of the present study is to answer this question by assessing
50 whether and to what extent anthropogenic warming has contributed to the occurrence
51 probability of the 2021 NWP concurrent marine and terrestrial summer heat (Perkins-
52 Kirkpatrick et al. 2019; Amaya et al. 2021).



53
 54 **Fig. 1.** (a) SSTA (°C) and SATA (inset; °C) patterns in July 2021. The main hosting cities of the
 55 2020 Tokyo Olympics are marked by pentagrams. The black and blue rectangles encompass the
 56 NWP and NEA regions, respectively. (b) The July NWP SSTA (blue solid line; °C) and NEA
 57 SSTA (pink bar; °C) during 1961–2021. The 2- σ levels are marked by dashed lines. Values for
 58 the years 1978 and 2021 are shown as well. (c) Anomalies of 2021 July 500-hPa geopotential
 59 height (with zonal mean removed; shadings; gpm) and 850-hPa horizontal wind (vectors; m s⁻¹)
 60 from ERA5. The green rectangle indicates the target circulation region. (d) Same as (c), but
 61 for the year 1978. (e) Statistical dependence between July NWP SSTA and NEA SATA. Red
 62 dots indicate the original data, and blue dots the linearly detrended ones. The year 2021 is
 63 marked by pentagrams and the 90% percentiles are highlighted. The linear regression model,
 64 the Pearson correlation coefficient (r), and the proportion of the variance of y explained by x
 65 (R^2) are also shown. (f) The best estimate and 90% confidence interval of the scaling factors
 66 (derived from the ROF) for ALL, ANT, and NAT forcings in July NWP SSTA and NEA SATA.

67

68 **Data.** We focus on July mean temperature anomalies since both marine and terrestrial
 69 heat occurred in July 2021. We find modest differences of about 0.1°C exist in July
 70 SSTA among different data sets (Fig. S1). To minimize uncertainties, we calculate the
 71 ensemble mean of three monthly data sets (HadISST, Rayner et al. 2003; ERSST v5,

72 Smith et al. 2008; COBESST v2, Hirahara et al. 2014) as the best observational SSTA
73 estimate. We use the monthly gridded Berkeley Earth land-surface temperature (BEST,
74 Rohde et al. 2013) to calculate SATA over terrestrial NEA. We also use monthly 850-
75 hPa horizontal wind and 500-hPa geopotential height data from the ERA5 reanalysis
76 (Hersbach et al. 2020). We focus our analyses on 1961–2021 and the results are
77 generally robust against different choices of studying periods and climate norms.

78 We use model outputs of monthly SAT, surface temperature, and geopotential heights
79 from the CMIP6 archive to investigate the influences of anthropogenic forcings (ANT;
80 Eyring et al. 2016). To improve the sampling of internal climate variability, we require
81 each model to have at least three ensemble members and 500 years of preindustrial
82 control (pi-CTL) run. Ten models satisfy this criterion, which produce historical
83 simulations until 2014 with all forcings (ALL; hist-All) and until 2020 with natural-
84 only forcings (NAT; hist-Nat), and future projections unfolding along two different
85 Shared Socioeconomic Pathways (SSP2-45 and SSP5-85) (Table S1). Since SSP2-45
86 forcings were employed in hist-Nat simulations for 2015–2020 (Gillett et al. 2021), we
87 extend the hist-All simulations with corresponding SSP2-45 experiments for this period.
88 All the data are bilinearly interpolated to a $1^\circ \times 1^\circ$ grid from their respective original grids
89 and the results are generally robust against different interpolation methods.

90 **Methods.** Accounting for potential biases in the simulated responses to forcings, we
91 first perform calibration analysis using regularized optimal fingerprinting method (ROF;
92 Allen and Stott 2003; Ribes et al. 2013). Briefly, based on a total-least-squares
93 algorithm, this technique regresses the observed change onto the simulated responses
94 to different forcings and accounts for the noise in the model responses associated with
95 internal variability (Note S1). After ensuring the detectability of ANT, we use the ROF-
96 derived regression coefficient (i.e., scaling factor) of ANT to calibrate historical and
97 future ANT signals. We add these observationally-constrained ANT signals to non-
98 overlapping 60-year chunks of unforced series (pi-CTL simulations) to create plausible
99 realizations of NWP SSTA and NEA SATA (Sun et al. 2014). We compare the

100 constructed evolutions involving anthropogenically-forced warming with the unforced
101 ones to investigate the overall contribution of human influences to the event risk. To
102 reduce uncertainties related to statistical methods, here we use three different
103 approaches to estimate the joint probabilities of occurrence of 2021-like spatially
104 concurrent heat extremes with and without human influences (P_{ANT} and P_{CTL}) by:

105 I) empirically counting the occurrence of the events with SSTA and SATA exceeding
106 their respective thresholds (i.e., the 1978 event; Figs. 1b, 1e);

107 II) using a Gaussian copula to model the co-dependence of SSTA and SATA and derive
108 bivariate exceedance probability (Nelsen 2007);

109 III) using a Gaussian bivariate kernel density estimator (GBKDE; Terrell and Scott
110 1992).

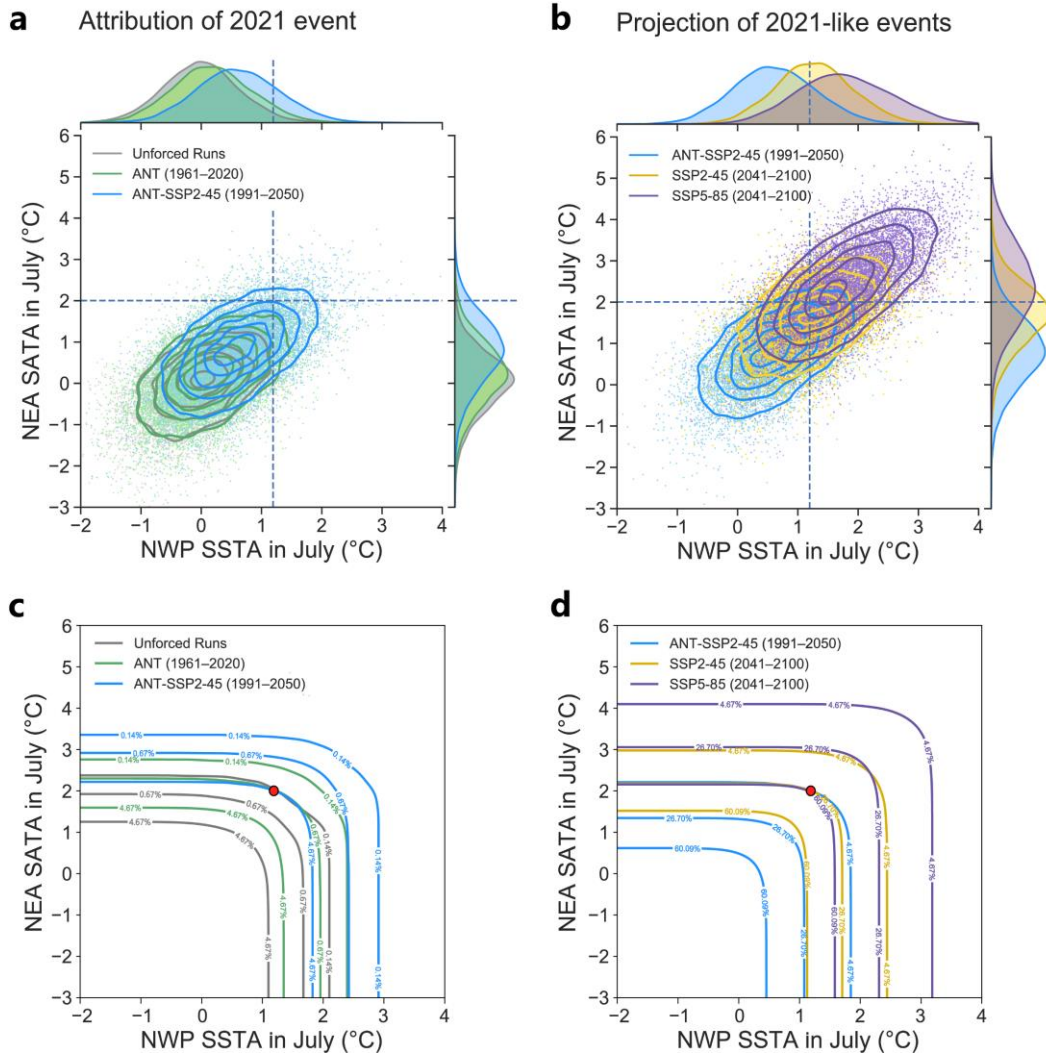
111 We compute the probability ratio ($PR=P_{ANT}/P_{CTL}$) and its 5–95% uncertainty range via
112 bootstrapping 1000 times (Efron and Tibshirani 1994).

113 **Results.** Both the July 2021 NWP SSTA and NEA SATA are above two standard
114 deviations (σ) and are the first and second warmest since 1961, respectively (Fig. 1b).
115 The mid-latitude lobe of the positive Pacific–Japan teleconnection pattern serves as a
116 common driver of sunny and hot weather over subtropical NWP (Figs. 1c, d; Noh et al.
117 2021). As a result, the marine and terrestrial heat are significantly spatially related (Fig.
118 1e). Mean anomalous warm air advection from NEA lands to NWP could strengthen
119 their correlation as well.

120 The ANT and NAT signals are jointly detectable in the observed SSTA and SATA
121 changes, whilst the scaling factors for NAT exhibit a much larger confidence interval
122 (Fig. 1f). The below-unity scaling factors for ANT indicate an overestimate of the
123 amplitude of simulated regional temperature responses to ANT in models (i.e., ‘hot
124 model’ bias; Hausfather et al. 2022). By altering the ANT signals to best match the
125 observed changes and adding them to the unforced simulations, we produce 154
126 plausible realizations of the 1961–2020 NWP SSTA and NEA SATA evolutions. The

127 median σ of the 154 reconstructed SSTA and SATA series are 0.64°C and 0.80°C , close
128 to the observations (0.59°C and 0.97°C). The median Pearson correlation between them
129 is 0.58, consistent with the observed (0.62; Fig. 1e). These results suggest that the
130 simulated series faithfully reproduce the observed variability and statistical dependence
131 between NWP and NEA.

132 Using the unforced simulations and GBKDE, we estimate the occurrence probability of
133 2021-like NWP spatially concurrent marine and terrestrial summer heat without human-
134 induced warming to be 0.14% (0.09–0.21%) (Figs. 2a, c; Table 1). Due to the effects of
135 historical anthropogenic warming from 1961 to 2020, the marginal probability
136 distributions of NWP SSTA and NEA SATA shift toward high levels (Fig. 2a). The joint
137 exceedance probability derived from the corresponding plausible realizations is 0.67%
138 (0.53–0.81%) and the associated PR is estimated to be 4.63 (3.21–7.31), which signifies
139 that historical human-induced warming has already led to about a fourfold growth in
140 the risk of 2021-like spatially concurrent heat events (Fig. 2c; Table 1). However, the
141 background warming level around 2021 should be higher than the 1961–2020 average.
142 Thus, we repeat the analysis but add the calibrated anthropogenic warming component
143 over 1991–2050 (centered on 2021) to the unforced data (referred to as ANT-SSP2-45).
144 The estimated PR increases to 32.23 (21.98–51.78), which means current human-
145 induced warming has resulted in approximately a 30-fold increase in the event's
146 occurrence probability (Fig. 2c; Table 1). We consider the observationally-constrained
147 ANT signals over 2041–2100 (centered on 2070) to represent future warming in the
148 second half of the 21st century (Figs. 2b, d). Compared to the current level, future
149 similar events would become approximately 6- and 13-fold more likely under SSP2-45
150 and SSP5-85, respectively (Table 1). The 2021-like spatially concurrent summer heat
151 would become roughly once-in-4-year and once-in-1.5-year events in these scenarios,
152 respectively. Similar conclusions can be drawn from the other two statistical approaches,
153 albeit with some quantitative differences (Table 1).



154

155 **Fig. 2.** (a) The marginal and joint probability distributions of July mean NWP SSTA and NEA
 156 SATA in the unforced (gray), reconstructed ANT (1961–2020, green) and ANT-SSP2-45 (1991–
 157 2050, blue) plausible realizations. The horizontal and vertical dashed lines indicate the NWP
 158 SSTA and NEA SATA thresholds (i.e., the 1978 event). From innermost to outermost, the 5th,
 159 25th, 50th, 75th, and 95th percentiles of the distributions (contours) are estimated using a GBKDE.
 160 (b) Same as (a), but for ANT-SSP2-45 (1991–2050, blue), and the reconstructed SSP2-45 (gold)
 161 and SSP5-85 (purple) plausible realizations over 2041–2100. (c) Joint occurrence risk curves
 162 for the unforced (gray), reconstructed ANT (1961–2020, green), and ANT-SSP2-45 (1991–
 163 2050, blue) plausible realizations using exceedance probabilities [i.e., $P(X > x, Y > y)$]. The
 164 colored numbers embedded in the curves represent joint exceedance probabilities. The red dot
 165 marks the joint thresholds. (d) Same as (c), but for ANT-SSP2-45 (1991–2050, blue), and the
 166 reconstructed SSP2-45 (gold) and SSP5-85 (purple) plausible realizations over 2041–2100.

167 **Table 1.** The marginal (for SSTA and SATA, based on Gaussian fitting) and joint exceedance
 168 probability (estimated via three statistical methods) exceeding the observed 2021 thresholds in
 169 different reconstructed plausible realizations. The PRs and their corresponding 5–95% ranges
 170 are shown as well.

Simulations/PRs	Marginal probability (SSTA)	Marginal probability (SATA)	Joint exceedance probabilities estimated by three different statistical approaches		
			Empirical	Gaussian-Copula	GBKDE
I. Unforced	2.85% (2.67–3.05%)	0.40% (0.36–0.45%)	0.14% (0.08–0.21%)	0.11% (0.09–0.13%)	0.14% (0.09–0.21%)
II. ANT (1961–2020)	6.36% (6.06–6.73%)	1.43% (1.32–1.55%)	0.58% (0.47–0.71%)	0.58% (0.52–0.63%)	0.67% (0.53–0.81%)
PR (II/I)	2.23 (2.05–2.43)	3.57 (3.13–4.10)	4.17 (2.83–7.14)	5.20 (4.78–5.71)	4.63 (3.21–7.31)
III. ANT-SSP2-45 (1991–2050)	20.22% (19.63–20.82%)	7.68% (7.35–8.04%)	4.36% (3.99–4.72%)	4.57% (4.35–4.83%)	4.67% (4.30–5.04%)
PR (III/I)	7.05 (6.55–7.63)	19.28 (17.02–21.82)	31.38 (21.18–55.81)	41.86 (37.76–46.75)	32.23 (21.98–51.77)
IV. SSP2-45 (2041–2100)	55.07% (54.37–55.80%)	33.78% (33.14–33.44%)	25.52% (24.79–26.35%)	25.88% (25.30–26.48%)	26.70% (25.90–27.69%)
PR (IV/III)	2.73 (2.64–2.82)	4.40 (4.19–4.61)	5.86 (5.46–6.34)	5.66 (5.46–5.86)	5.72 (5.32–6.21)
V. SSP5-85 (2041–2100)	77.40% (76.88–77.96%)	65.72% (65.08–66.36%)	58.84% (58.02–59.69%)	59.34% (58.67–60.02%)	60.09% (59.00–61.22%)
PR (V/III)	3.83 (3.72–3.94)	8.54 (8.16–8.93)	13.49 (12.53–14.73)	12.93 (12.38–13.63)	12.88 (11.92–14.12)

171

172 The increases in the frequency of 2021-like spatially-compounding heat events may
 173 primarily arise from shifts in marginal distribution of NWP SSTA and NEA SATA, with
 174 the changing dependence structure contributing little (Figs. 2a, b). This connotes that

175 their physical linkage via the common anticyclonic pattern has not been and would not
176 be changed by anthropogenic warming. To test this hypothesis, we compute the pattern
177 correlation coefficients (r) between July 2021 500-hPa geopotential height anomalies
178 (with zonal mean removed; Z500') from ERA5 and July Z500' from hist-All (hist-Nat,
179 SSP2-45) simulations during a 60-years period over the target circulation region (green
180 box in Fig. 1c; 125–180°E; 35–55°N). The composite circulations in the analog Z500'
181 patterns that resemble the observed in July 2021 ($r > 0.5$) bear notable similarities among
182 the hist-All, hist-Nat, and SSP2-45 ensembles (Fig. S2a, b, and c). Moreover, there is
183 no significant shift in the frequency of analog Z500' patterns ($r \geq 0.5$) due to historical
184 and future anthropogenic forcings (Fig. S2d). Similar results could be achieved when
185 directly comparing the July Z500' averaged over the target circulation region in the hist-
186 All, hist-Nat, and SSP2-45 simulations (Fig. S2e). In addition, the result is robust
187 against slightly changed target circulation regions and different reanalysis data (figure
188 omitted).

189 **Conclusions.** With the aid of CMIP6 multi-model ensemble simulations and optimal
190 fingerprinting detection technique, we find that current human-induced warming has
191 led to about a 30-fold increase in the occurrence probability of a record-breaking
192 spatially concurrent marine and terrestrial summer heat that occurred across the NWP
193 in July 2021. Its occurrence risk in the second half of the 21st century is projected to be
194 at least six times the 2020s level, even under a moderate emission scenario. Results
195 imply that the compounding effects of unprecedented spatially simultaneous heat on
196 agricultural and fishery productions in the NWP and its nearby lands may increase and
197 substantial cuts in emissions are paramount to reduce the risks. This study may shed
198 light on the ongoing efforts attributing less explored yet potentially more impactful
199 spatially compounding events to anthropogenic climate change.

200

201 **Acknowledgments**

202 This study was supported by the National Natural Science Foundation of China
203 (42025503) and the Strategic Priority Research Programme of the Chinese Academy of
204 Sciences (XDA20020201).

205

206 **Data Availability**

207 All the data that support the findings are publicly available. The gridded Berkeley Earth
208 Surface Temperature dataset is available at <http://berkeleyearth.org/data>. The HadISST,
209 ERSST v5, and COBESST v2 data sets can be downloaded from their official websites
210 <https://www.metoffice.gov.uk/hadobs/hadisst/>,
211 [https://data.noaa.gov/dataset/dataset/noaa-extended-reconstructed-sea-surface-](https://data.noaa.gov/dataset/dataset/noaa-extended-reconstructed-sea-surface-temperature-ersst-version-5)
212 [temperature-ersst-version-5](https://data.noaa.gov/dataset/dataset/noaa-extended-reconstructed-sea-surface-temperature-ersst-version-5), and [https://data.noaa.gov/dataset/dataset/cobe-sst2-sea-](https://data.noaa.gov/dataset/dataset/cobe-sst2-sea-surface-temperature-and-ice)
213 [surface-temperature-and-ice](https://data.noaa.gov/dataset/dataset/cobe-sst2-sea-surface-temperature-and-ice), respectively. The model outputs in CMIP6 can be
214 accessed at <https://esgf-node.llnl.gov/projects/cmip6/>. The ERA5 reanalysis data can
215 be secured from <https://www.ecmwf.int/en/forecasts/datasets/reanalysis-datasets/era5>
216 on registration.

217

218 **References**

- 219 Allen, M. R., and P. A. Stott, 2003: Estimating signal amplitudes in optimal fingerprinting, part
220 I: theory. *Clim. Dyn.*, **21**, 477–491.
- 221 Amaya, D. J., and Coauthors, 2021: Are long-term changes in mixed layer depth influencing
222 North Pacific marine heatwaves? *Bull. Amer. Meteor. Soc.*, **102**, S59–S66.
- 223 Efron, B., and R. Tibshirani, 1994: *An Introduction to the Bootstrap*. CRC Press, 456 pp.
- 224 Eyring, V., S. Bony, G. A. Meehl, C. A. Senior, B. Stevens, R. J. Stouffer, and K. E. Taylor,
225 2016: Overview of the Coupled Model Intercomparison Project Phase 6 (CMIP6)
226 experimental design and organization. *Geosci. Model Dev.*, **9**, 1937–1958.
- 227 Gillett, N. P., and Coauthors, 2021: Constraining human contributions to observed warming
228 since the pre-industrial period. *Nat. Clim. Chang.* **11**, 207–212.

- 229 Hausfather, Z., K. Marvel, G. A. Schmidt, J. W. Nielsen-Gammon, and M. Zelinka, 2022:
230 Climate simulations: recognize the ‘hot model’ problem. *Nature* **605**, 26–29.
- 231 Hersbach, H., and Coauthors, 2020: The ERA5 global reanalysis. *Q. J. R. Meteorol. Soc.*, **146**,
232 1999–2049.
- 233 Hirahara, S., M. Ishii, and Y. Fukuda, 2014: Centennial-scale sea surface temperature analysis
234 and its uncertainty. *J. Clim.*, **27**, 57–75.
- 235 Kuroda, H., and T. Setou, 2021: Extensive marine heatwaves at the sea surface in the
236 northwestern Pacific Ocean in summer. *Remote Sens.*, **13**, 3989.
- 237 Kuroda, H., T. Azumaya, T. Setou, and N. Hasegawa, 2021: Unprecedented outbreak of harmful
238 algae in Pacific coastal waters off southeast Hokkaido, Japan, during late summer 2021
239 after record-breaking marine heatwaves. *J. Mar. Sci. Eng.*, **9**, 1335.
- 240 Nelsen, R. B., 2007: An introduction to copulas. Springer Science & Business Media.
- 241 NOAA National Centers for Environmental Information, State of the Climate: Monthly Global
242 Climate Report for July 2021, published online August 2021, retrieved on May 17, 2022,
243 from <https://www.ncei.noaa.gov/access/monitoring/monthly-report/global/202107>.
- 244 Noh, E., and Coauthors, 2021: The role of the Pacific-Japan pattern in extreme heatwaves over
245 Korea and Japan. *Geophys. Res. Lett.*, **48**, e2021GL093990.
- 246 Perkins-Kirkpatrick, S. E., and Coauthors, 2019: The role of natural variability and
247 anthropogenic climate change in the 2017/18 Tasman Sea marine heatwave. *Bull. Amer.*
248 *Meteor. Soc.*, **100**, S105–S110.
- 249 Rayner, N., and Coauthors, 2003: Global analyses of sea surface temperature, sea ice, and night
250 marine air temperature since the late nineteenth century. *J. Geophys. Res.*, **108**, 4407.
- 251 Ribes, A., S. Planton, and L. Terray, 2013: Application of regularised optimal fingerprinting to
252 attribution. Part I: method, properties and idealised analysis. *Clim. Dyn.*, **41**, 2817–2836.
- 253 Rohde, R., and Coauthors, 2013: A new estimate of the average earth surface land temperature
254 spanning 1753 to 2011. *Geoinfor. & Geostat.: An Overview*, **1**, 1–7.
- 255 Smith, T. M., R. W. Reynolds, T. C. Peterson, and J. Lawrimore, 2008: Improvements to
256 NOAA's historical merged land-ocean surface temperature analysis (1880–2006). *J. Clim.*,
257 **21**, 2283–2296.
- 258 Sun, Y., and Coauthors, 2014: Rapid increase in the risk of extreme summer heat in Eastern
259 China. *Nat. Clim. Chang.*, **4**, 1082–1085.
- 260 Terrell, G. R., and D. W. Scott, 1992: Variable kernel density estimation. *Ann. Stat.*, **20**, 1236–
261 1265.

- 262 Zscheischler, J., and Coauthors, 2020: A typology of compound weather and climate events.
263 *Nat. Rev. Earth Environ.* **1**, 333–347.